Eur. Phys. J. D **20**, 619–626 (2002)
DOI: 10.1140/epjd/e2002-00153-8

THE EUROPEAN PHYSICAL JOURNAL D

# Photo-induced reactions of hemin$^+$(DMSO)$_n$ clusters (n = 0–3) produced with electrospray ionization

S. Nonose, H. Tanaka, N. Okai, T. Shibakusa, and K. Fuke[a]

Department of Chemistry, Faculty of Science, Kobe University, Kobe 657-8501, Japan

Received 10 May 2002 / Received in final form 24 June 2002
Published online 13 September 2002 – 

**Abstract.** Photo-induced reaction of [Fe(III)-protoporphyrin]$^+$ (hemin$^+$) ions solvated with dimethylsulfoxide (DMSO) is investigated by using a tandem mass spectrometer with electrospray ionization. We measure the photodissociation yields of mass-selected hemin$^+$(DMSO)$_n$ clusters for $n = 0$–3 in the energy region of 15 800–28 200 cm$^{-1}$. The mass spectra of the fragment ions show the $\beta$-cleavage of carboxymethyl groups in addition to the evaporation of solvent molecules. Yield of the $\beta$-cleavage reaction is found to depend strongly on the excitation energy and the number of solvent molecules. We also examine the metastable decomposition of the clusters following primary mass selection and determine the incremental solvent binding energies and internal energies for the clusters using evaporative ensemble model. From these results, we investigate the reaction mechanism of $\beta$-cleavage of hemin$^+$ ion.

**PACS.** 36.40.-c Atomic and molecular clusters – 73.22.-f Electronic structure of nanoscale materials: clusters, nanoparticles, nanotubes, and nanocrystals

## 1 Introduction

Spectroscopy of the gas-phase clusters containing metal ions has been studied extensively to bridge the gap between the gas-phase and the condensed-phase metal ions [1–5]. Infrared vibrational predissociation spectroscopy has been proven to be the useful technique to determine the solvation structure around metal ions [6,7]. Photoionization, photodissociation, and photoelectron spectroscopies of the solvent clusters containing alkali metal atoms have also been the subject of intensive studies [8–14]. These studies indicate a spontaneous ionization of an alkali atom in small clusters; the metal atom is gradually ionized to form a one-center ion-pair state. Photodissociation spectroscopy of the clusters containing alkaline-earth metal ion has been also investigated [15–18]. The results provide information on the microscopic solvation of metal ions. Recent advances in soft desorption and ionization techniques have made possible to introduce intact nonvolatile molecules into the gas phase. In particular, electrospray ionization (ESI) offers new means to transfer molecular ions to the gas phase without destruction [19–23]. ESI mass spectrometry is now routinely used to determine the molecular weights of large nonvolatile molecules. Several groups have applied ESI to spectroscopic studies of the gas-phase cluster ions, such as $Fe^{2+}(bpy)_3(CH_3OH)_n$ [24], $Ni^{2+}(H_2O)_n$ [25], and halogenometallate anions [26].

Metalloporphyrins comprise an important class of molecules that serve nature in variety of ways [27–29]. They are active sites of numerous proteins whose functions range from oxygen transport and storage (hemoglobin, myoglobin) to electron transport (cytochrome c, cytochrome oxidase) and energy conversion (chlorophyll). Additionally, porphyrins have been proven to be efficient photosensitizers and catalysts in a number of chemical and photochemical systems. Such diverse functions of metalloporphyrins continue to be focus of extensive spectroscopic investigations in condensed phase. The chemical reactivity and reaction dynamics of metalloporphyrins in condensed phase are strongly influenced by the surrounding solvent environments. In order to investigate the microscopic solvation and the dynamics of reaction, metalloporphyrins are introduced into the gas phase as ions. Collision-activated dissociation of porphyrins has been investigated extensively by tandem mass spectrometry. These studies indicate that a $\beta$-cleavage is the most important process for the dissociation of porphyrins [19,30].

In the present work, the photo-induced reaction of dimethylsulfoxide (DMSO) clusters containing [Fe(III)-protoporphyrin]$^+$ (hemin$^+$) ions are investigated in order to clarify the mechanism of the $\beta$-cleavage reaction. DMSO is used as solvent, because it has a large dipole moment (2.54 Debye) and strongly interacts with ionic species in the gas phase as well as in solution. Therefore, extensive solvation effects would be expected for the reactions of hemin$^+$ ion in DMSO clusters. The photodissociation yield of mass-selected hemin$^+$(DMSO)$_n$ clusters

[a] e-mail: fuke@kobe-u.ac.jp

($n$ = 0–3) is examined in the energy region of 15 800–28 200 cm$^{-1}$. We also measure metastable decomposition yields to estimate incremental binding energies. On the basis of these results, we discuss the mechanisms of the photo-induced reactions of solvated hemin$^+$ ion.

## 2 Experimental

Details of the experimental apparatus used in the present study have been described elsewhere [31]. Briefly, the system consists of an ESI source and a tandem mass spectrometer with octapole ion beam guides. Hemin$^+$(DMSO)$_n$ ions are produced by ESI of a dilute solution of Fe(III)-protoporphyrin chloride (hemin chloride, Wako Chemicals) in methanol-dichloromethane (1:1 v/v) mixture including dimethylsulfoxide (DMSO) (1.0%). A mechanical pump for a liquid chromatography delivers solution to an electrospray needle. Optimum intensity and stability of ion signals are obtained with a $2 \times 10^{-4}$ M solution of hemin, which is delivered to the needle tip at a rate of 0.01 ml/min. The electrospray needle is biased at 4.5–5.0 kV with respect to a platinum aperture of 0.1 mm in diameter. A flow of 10–800 ml/s of dry nitrogen is maintained through the atmospheric pressure ion source [22,23]. The flow continuously removes solvent vapor produced by the electrospray. Ions produced by the electrospray in the atmospheric region drift under the influence of the electric field towards the interface plate, and enter the interface region through a hole (4 mm in diameter) on the interface plate. The interface plate is heated up to about 350 K. Ions formed in the ESI source are admitted into the first vacuum chamber, which is evacuated by a 3 000 l/s diffusion pump (ULVAC, ULK-10A). The ion beam is then pass through a stainless-steel skimmer, and is focused by electrostatic lenses into the first octapole-ion-beam guide (OPIG1). The OPIG1 is connected directly to the first quadrupole mass spectrometer (QMASS1; ABB EXTEL, 664901) in the second chamber evacuated by a 2 000 l/s diffusion pump (Edwards, Diffstak 250/2000C). The mass-selected ions emerging from the QMASS1 are deflected 90° by a first quadrupole ion deflector (QDF1), and are admitted into the second octapole-ion-beam guide (OPIG2). High transmission efficiency for slow ions is accomplished by applying a radio frequency (RF) field to the OPIGs. The OPIG2 in the third chamber is jointed to the first and second quadrupole ion deflectors. The third chamber is evacuated with a 400 l/s turbo molecular pump (SEIKO SEIKI, STP-400). The difference of dc voltages between the skimmer and the OPIG2 corresponds to the kinetic energy of ions passing through OPIG2. The retention time of hemin$^+$ ion (617 amu) in OPIG2 is 350 $\mu$s. After passing through OPIG2, the parent and product ions are deflected 90° by the second quadrupole ion deflector (QDF2), and are admitted into the second quadrupole mass spectrometer (QMASS2) (ABB EXTEL, 652601). The ions are detected by a channeltron electron multiplier equipped with a conversion dynode. By adjusting dc voltages of OPIG2 and QDF2, the collection efficiency of product ions having a sizable kinetic energy spread is maximized. Signals from the detector are fed into a current amplifier and are averaged by a digital storage oscilloscope.

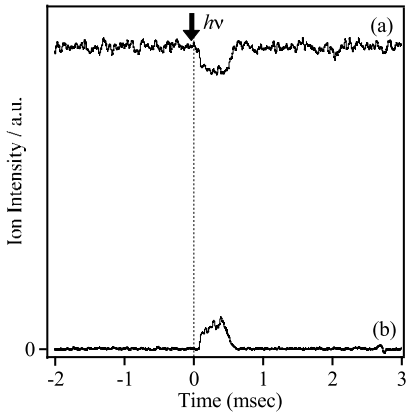


**Fig. 1.** Time profiles of the parent cluster ion (hemin$^+$, 617amu) (a) and the product ion (499 amu) (b) before and after the irradiation of the photolysis laser (28 200 cm$^{-1}$). Depletion of the parent ion is observed at 100–450 $\mu$s after the irradiation. The product ion is observed in the same time period as the depletion of the parent ion.

Photodissociation spectra are recorded by measuring depletion yield of the parent cluster ions as a function of the photolysis energy. The laser beam is introduced into OPIG2 colinearly and counterpropergatedly with the ion beam. We use the following lasers as the photolysis light source; the 2nd or the 3rd harmonic of a YAG laser and the output of an optical parametric oscillator (Spectra Physics, MOPO-730). Figure 1 shows (a) the depletion of a parent ion (hemin$^+$, 617 amu) and (b) the production of a daughter ion (499 amu) as a function of the time after the irradiation of the photolysis laser (28 200 cm$^{-1}$). The latter ions are produced by a $\beta$-cleavage of carboxymethyl groups as mentioned in the next section. The depletion of the parent ions is observed at 100 $\mu$s after the irradiation with a duration time of 350 $\mu$s. Daughter ions are observed with the same time period as that of the depletion of the parent ions. This time period corresponds to the retention time of OPIG2, and is consistent with the value estimated by using the velocity of the ions in OPIG2. Relative photodissociation cross-section, $\sigma_{\rm rel}$, is determined by

$$\sigma_{\rm rel} = \ln(I_{\rm off}/I_{\rm on}), \tag{1}$$

where $I_{\rm on}$ and $I_{\rm off}$ are the signal intensities of ions in the mass spectrum with and without irradiating the photolysis laser beam, respectively. Laser fluence is attenuated to less than 3 mJ cm$^{-2}$ to avoid multiphoton absorption. We carefully measure the laser fluence dependence of the photodepletion yield for the parent ions in 1–10 mJ cm$^{-2}$, and confirm that $\sigma_{\rm rel}$ is propotional to the laser fluence. We also check that the distribution of product ions depends not on the laser fluence. Therefore, the multiphoton processes are considered to be not significant in the present experiments, though hemin$^+$ has the large absorption cross-section.

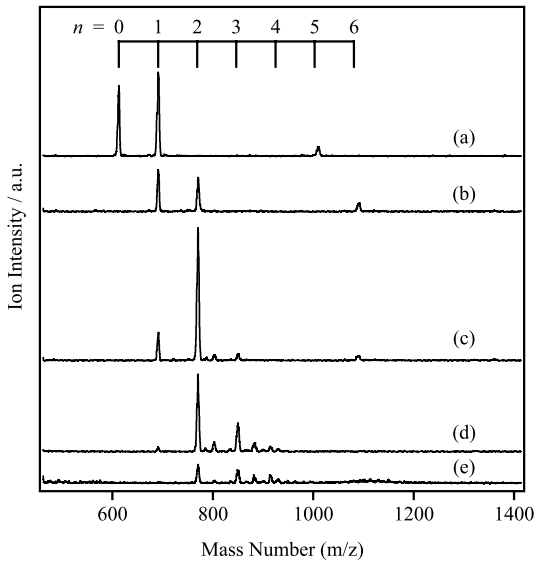


**Fig. 2.** The mass spectra of solvated hemin cluster ions, hemin$^+$(DMSO)$_n$ ($n$ = 0−6), produced by ESI with various flow rates of nitrogen in the interface region. The flow rates of nitrogen are 800 ml/min (a), 200 ml/min (b), 100 ml/min (c), 50 ml/min (d), and 10 ml/min (e), respectively.

## 3 Results and discussion

Figure 2 shows the mass spectra of solvated hemin cluster ions, hemin$^+$(DMSO)$_n$, produced at various flow rates of nitrogen in the interface region. As shown in Figure 2e, very weak signals of the hemin$^+$(DMSO)$_n$ ($n$ = 2−5) clusters are observed at the lowest $N_2$ flow rate. Very small peaks appeared in between those of hemin$^+$(DMSO)$_n$ correspond to the clusters containing methanol molecules. With increasing the flow rate, the larger cluster ions disappear and smaller cluster ions are produced efficiently. At the highest flow rate, hemin$^+$ and hemin$^+$(DMSO)$_1$ are observed most strongly as seen in Figure 2a. These results clearly show that the intensity and mass distribution of the ionic species produced by ESI depend strongly on the flow rate. They also depend on the temperature of the interface plate, and the electric field strength of high-pressure zone in the first chamber [22,23]: high temperature and high flow rate enhance desolvation.

### 3.1 Incremental binding energies of hemin$^+$(DMSO)$_n$ clusters

For the analytical applications of ESI source, special attention has not been paid to characterize the internal energy and temperature of produced ions [20–23,30]. However, for spectroscopic investigations, it is important to know the internal energy of the ions. In order to estimate the internal energy, we examine the metastable decomposition of hemin$^+$(DMSO)$_n$ clusters. These clusters may proceed the following dissociation processes between the initial mass selection and final detection

$$\begin{aligned}
\text{hemin}^+(\text{DMSO})_n &\xrightarrow{k_n(E_n)} \text{hemin}^+(\text{DMSO})_{n-1} \\
&\quad + \text{DMSO} \\
\text{hemin}^+(\text{DMSO})_{n-1} &\xrightarrow{k_{n-1}(E_{n-1})} \text{hemin}^+(\text{DMSO})_{n-2} \\
&\quad + \text{DMSO} \\
&\vdots \\
\cdots &\longrightarrow \cdots
\end{aligned} \tag{2}$$

where $k_n(E_n)$ is the dissociation rate of the solvated clusters as mentioned later. Incremental binding energies of DMSO and average internal energies of clusters are estimated by using an evaporative ensemble model developed for unimolecular decomposition of clusters [6,7,24,32]. In this model, it is assumed that the evaporation occurs by a sequential loss of neutral monomers and at least one molecule evaporates before the detection. The kinetic energy release accompanying with metastable decay is also assumed to be twice as large as the available energy per one active vibrational degree of freedom [7]. In the present experiment, the cluster ions exit the ESI source through the skimmer and enter the collision-free environments in QMASS1 ($5 \times 10^{-6}$ torr). Ions typically take about 200 $\mu$s to reach QMASS1, which provides the primary mass selection. Loss of one DMSO molecule occurs during the time (∼350 $\mu$s) to reach QMASS2 from QMASS1. The metastable decomposition including the loss of two solvent molecules is not observed in the present experiment. In Figure 3a, the metastable decay fractions are plotted as a function of cluster size. The results indicate that the increase in the metastable fractions with increasing the cluster size is a characteristic of the evaporative ensembles.

According to the classical RRK theory, the unimolecular dissociation rate constant for hemin$^+$(DMSO)$_n$ is given by

$$k_n(E_n) = A\left(\frac{E_n - V_n}{E_n}\right)^{L(n)-1} \tag{3}$$

where $A$ is the frequency prefactor in s$^{-1}$, $E_n$ is the internal energy of the cluster, $V_n$ and $L(n)$ are the binding energy of $n$th DMSO molecule and the number of active or effective oscillators in the cluster. As for the frequency prefactor, Lisy and co-workers have predicted a number such as $4 \times 10^{12}$ s$^{-1}$ for Cs$^+$(CH$_3$OH)$_n$ [7]. We also calculate the rate with changing the frequency prefactor by a factor of 10, and find that the internal energies of the clusters change by less than 20%. The results indicate that the internal energy is not sensitive to the prefactor. Thus we use the same value for $A$ in the present calculations. The active oscillator includes both the intermolecular modes and the low-frequency vibrational modes in hemin$^+$ and DMSO molecules. An appropriate value for $L(n)$ to evaluate the RRK rate constant is estimated as follows. For hemin$^+$(DMSO)$_n$, the number of the intermolecular vibrational modes is $6n$. DMSO molecules in the clusters have the internal rotation of methyl groups as $2n$. The number of low-frequency modes for the skeletal vibrations in

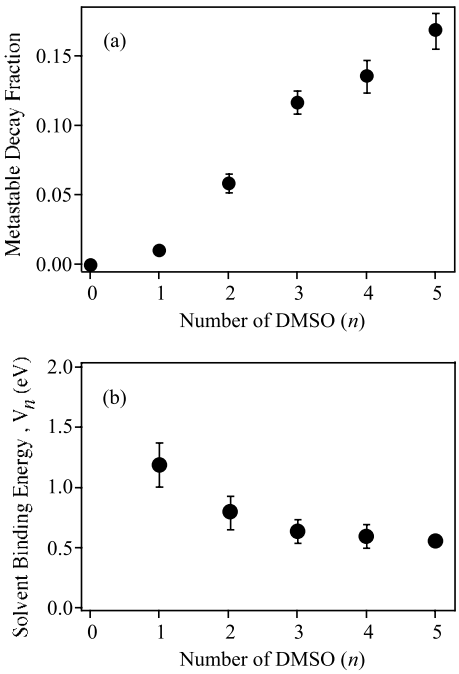


**Fig. 3.** (a) Decay fractions for the metastable decomposition of hemin$^+$(DMSO)$_n$ clusters by loss of one DMSO molecule. (b) Incremental binding energies of DMSO molecules in hemin$^+$(DMSO)$_n$ clusters estimated by evaporative ensemble model.

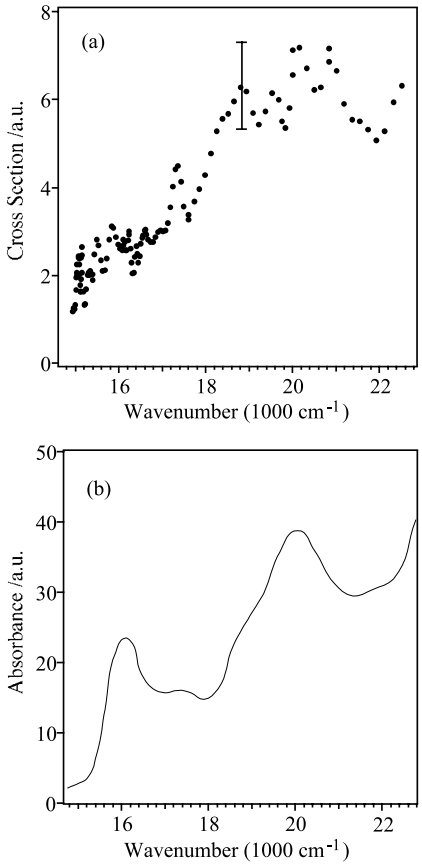


**Fig. 4.** (a) Photodepletion spectrum of hemin$^+$(DMSO)$_1$ complex in the region of 15 100–22 700 cm$^{-1}$. Absorption spectrum of hemin chloride in DMSO solution (b) is also shown for comparison.

porphyrin below 350 cm$^{-1}$, which are out-of-plane bending modes, has been predicted to be 6 [33]. Hemin$^+$ ion has 14 intramolecular rotations of methyl, methylene, and –OH groups. Thus, the number of low-frequency modes in the hemin$^+$(DMSO)$_n$ clusters is expressed as

$$L(n) = 8n + 20. \quad (4)$$

By using the RRK rate constants (Eq. (3)), iterative evaluations are performed until agreement is reached between the calculated and observed fractions for metastable decay. In order to estimate the absolute values of $V_n$, the incremental binding energy of $n = 6$ is assumed to be equal to the bulk enthalpy of vaporization of DMSO (0.548 eV) [34]. With this assumption, the lower limit of $V_n$ are calculated to be 1.2±0.25, 0.8±0.15, 0.64±0.10, 0.60±0.10, and 0.56±0.10 eV for $n = 1$–5, respectively, as shown in Figure 3b. The $V_n$ values decrease monotonously with increasing $n$. Kebarle and co-workers have determined the incremental binding energies of K$^+$(DMSO)$_n$ clusters to be 1.5, 1.2, 0.84, 0.67, 0.66, and 0.64 eV for $n = 1$–6, respectively, using high-pressure mass spectrometry [35]. They have also performed the theoretical calculations on the structure of K$^+$(DMSO)$_1$. The calculations predict that the most stable structure has K$^+$–O bond, and it is stabilized mostly by electrostatic interaction between K$^+$ and the large dipole moment of the S=O bond. The $V_n$ values for the hemin$^+$(DMSO)$_n$ clusters are slightly smaller than those for K$^+$(DMSO)$_n$. These results suggest that the bonding in hemin$^+$(DMSO)$_n$ is also mostly electrostatic interaction. The average internal energies for the hemin$^+$(DMSO)$_n$ clusters are calculated to be 1.6, 1.3, 1.2, 1.3, and 1.4 eV for $n = 1$–5, respectively. Though the distribution of energies in evaporative ensemble is not Boltzmann, a "temperature", $T_n$, is determined by distributing the average internal energy between the active modes [7,24]. The $T_n$ values are calculated to be 670, 400, 320, 300, and 280 K for $n = 1$–5, respectively. These results indicate that the cluster temperature decreases with increasing cluster size. This trend is consistent with the decrease of the incremental binding energies of the clusters as mentioned previously.

### 3.2 Photodissociation of hemin$^+$(DMSO)$_n$ clusters

Photodepletion spectrum of hemin$^+$(DMSO)$_1$ complex in the energy region of 15 100–22 700 cm$^{-1}$ is presented in Figure 4a. The spectrum is normalized to the fluence of the laser beam. The absorption spectrum of hemin chloride in DMSO solution is also shown in Figure 4b for comparison. Porphyrinic compounds show several absorption bands of moderate intensity in visible region, which are called as a $Q$ band. In addition to these bands, an extremely strong absorption band is observed at ∼25 000 cm$^{-1}$, which is called as a Soret band [36]. The nature of these

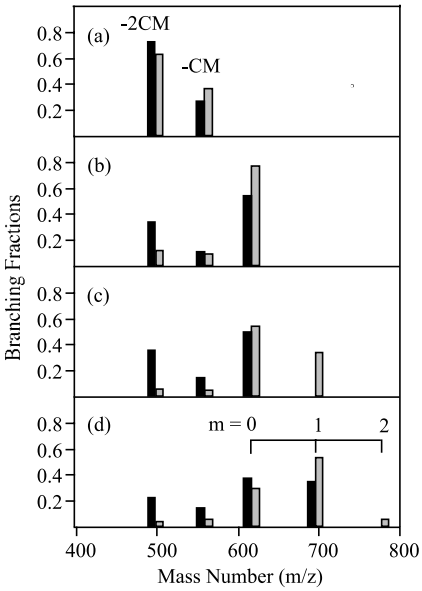


**Fig. 5.** Branching fractions of fragment ions produced by irradiation of hemin$^+$(DMSO)$_n$ ($n = 0$ (a) to 3 (d)). The striped and filled bars show the photoproducts generated with 2nd (18 800 cm$^{-1}$) and 3rd harmonic (28 200 cm$^{-1}$) of YAG laser, respectively. Cluster ions, hemin$^+$(DMSO)$_m$ ($0 \leq m < n$), and fragments of hemin$^+$ are observed as the product ions. Fragments of hemin$^+$, [hemin–$CH_2COOH$]$^+$ (558 amu) and [hemin–2($CH_2COOH$)]$^+$ (499 amu), are indicated by symbols, −CM and −2CM, respectively.

transitions in porphyrins and metalloporphyrins with $D_{4h}$ symmetry has been studied extensively [37–40]. In porphyrins, highest-occupied molecular orbital (HOMO) and lowest-unoccupied molecular orbital (LUMO) are $\pi$-type orbitals; HOMO ($1a_{1u}$), next-HOMO ($3a_{2u}$), and degenerated LUMO ($4e_g$) are called as "four orbitals" and are well separated from the other orbitals [36–38]. The $Q$ and Soret bands are ascribed to the promotion of the electrons from the $1a_{1u}$ and $3a_{2u}$ orbitals to the $4e_g$ orbital, respectively: the $Q$ and Soret bands correspond to the transitions to the $1E_u$ and $2E_u$ states, respectively [36]. The $Q$ band is split into two bands by a vibronic coupling; they are called as the $Q(0,0)$ and $Q(1,0)$ bands [38]. The broad bands at about 16 000 and 20 000 cm$^{-1}$ in Figure 4b correspond to the $Q(0,0)$ and $Q(1,0)$ bands. From the comparison with the solution spectrum, the broad maximum observed at about 20 000 cm$^{-1}$ in Figure 4a is assigned to the $Q$ band of hemin$^+$(DMSO)$_1$ complex.

Figure 5 shows the mass distributions of the fragment ions produced by the photolysis of hemin$^+$(DMSO)$_n$ ($n = 0$–3) clusters with the 2nd (18 800 cm$^{-1}$) and 3rd harmonic (28 200 cm$^{-1}$) of the YAG laser. The irradiations at 18 800 and 28 200 cm$^{-1}$ correspond to the excitations of the $1E_u$ and the $2E_u$ states, respectively. As shown in the figure, the fragment ions generated through the decomposition of hemin$^+$ ion are observed at 558 and 499 amu in addition to the evaporation products such as hemin$^+$(DMSO)$_m$ ($0 \leq m < n$). The mass spectra of porphyrinic compounds have been studied extensively. These studies have reported that the major decomposition process is $\beta$-cleavage:

$$[\text{porphyrin}-CH_2-R]^+ \rightarrow [\text{porphyrin}-CH_2\cdot]^+ + R\cdot \quad (5)$$

As discussed later, the occurrence of this reaction is well accord with the stability of the conjugated $\pi$ system, which allows wide delocalization of the positive charge [41]. From the comparison with the mass spectral data of porphyrinic compounds in the literatures [42–46], the product ions at 558 and 499 amu are assigned to the fragments, which loss one and/or two carboxymethyl groups, –$CH_2COOH$ (59 amu), by the $\beta$-cleavage reaction, respectively:

$$[\text{porphyrin}-CH_2CH_2COOH] \rightarrow [\text{porphyrin}-CH_2\cdot] + \cdot CH_2COOH. \quad (6)$$

In Figure 5, the fragment ions with loss of one and two –$CH_2COOH$ groups are designated as –CM and –2CM, respectively. With increasing the excitation energy from 18 800 to 28 200 cm$^{-1}$, the evaporation of DMSO and $\beta$-cleavage reaction are enhanced. Since we observe no indication of the reaction *via* an excited-state channel, the product ions are considered to be generated through the higher vibrational levels in the ground state repopulated *via* a fast internal conversion as follows; photoexcitation and repopulation of the higher vibrational levels of hemin$^+$ cluster ions in the ground state (Eq. (7)), subsequent sequential evaporation (Eq. (8)), and decomposition of hemin$^+$ (Eqs. (9, 10));

$$\text{hemin}^+(\text{DMSO})_n + h\nu \rightarrow [\text{hemin}^+(\text{DMSO})_n]^* \rightarrow [\text{hemin}^+(\text{DMSO})_n]^\ddagger \quad (7)$$

$$[\text{hemin}^+(\text{DMSO})_n]^\ddagger \rightarrow \text{hemin}^+(\text{DMSO})_m + (n-m)\text{DMSO} \rightarrow \ldots \rightarrow \text{hemin}^+ + n\text{DMSO} \quad (m \leq n) \quad (8)$$

$$[\text{hemin}^+(\text{DMSO})_n]^\ddagger \rightarrow [\text{hemin}^+-CH_2COOH](\text{DMSO})_n + \cdot CH_2COOH$$
$$[\text{hemin}^+-CH_2COOH](\text{DMSO})_n \rightarrow \ldots \rightarrow \text{hemin}^+-CH_2COOH + n\text{DMSO} \quad (9)$$

$$[\text{hemin}^+-CH_2COOH](\text{DMSO})_n \rightarrow [\text{hemin}^+-2(CH_2COOH)](\text{DMSO})_n + \cdot CH_2COOH$$
$$[\text{hemin}^+-2(CH_2COOH)](\text{DMSO})_n \rightarrow \ldots \rightarrow \text{hemin}^+-2(CH_2COOH) + n\text{DMSO} \quad (10)$$

where [hemin$^+$(DMSO)$_n$]$^*$ and [hemin$^+$(DMSO)$_n$]$^\ddagger$ represent the clusters in the initially excited state and the higher vibrational state on the ground-state surface, respectively. In the present study, solvated product ions such as [hemin$^+$–$k$($CH_2COOH$)](DMSO)$_m$ ($k$ = 1 or 2,

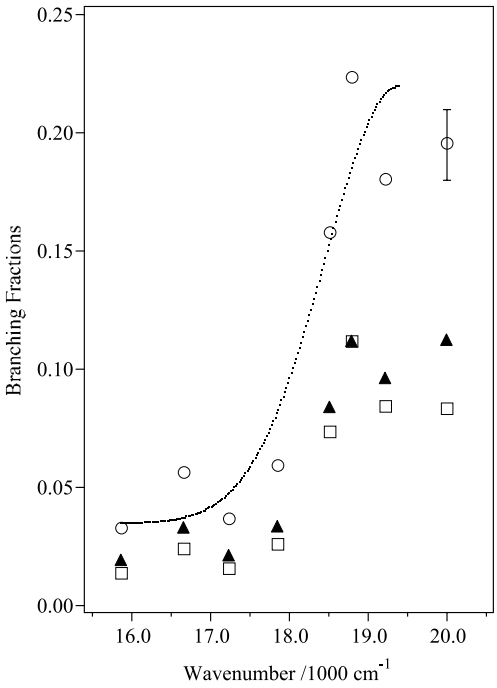


**Fig. 6.** Branching fractions, $R_t$, [$= (I[-2\mathrm{CM}]+I[-\mathrm{CM}])/\Sigma I_p$] for the photolysis of hemin$^+$(DMSO)$_1$ is shown as a function of the photon energy in the region of 15 800–20 000 cm$^{-1}$. Branching ratios, $R_1$ [$= I[-\mathrm{CM}]/\Sigma I_p$] and $R_2$ [$= I[-2\mathrm{CM}]/\Sigma I_p$], for the photolysis of the hemin$^+$(DMSO)$_1$ complex are also shown. $R_t$, $R_1$ and $R_2$ are presented as empty circles, filled triangles and empty squares, respectively. In order to estimate the position of the onset for $R_t$, the data points are fitted by a Gaussian function.

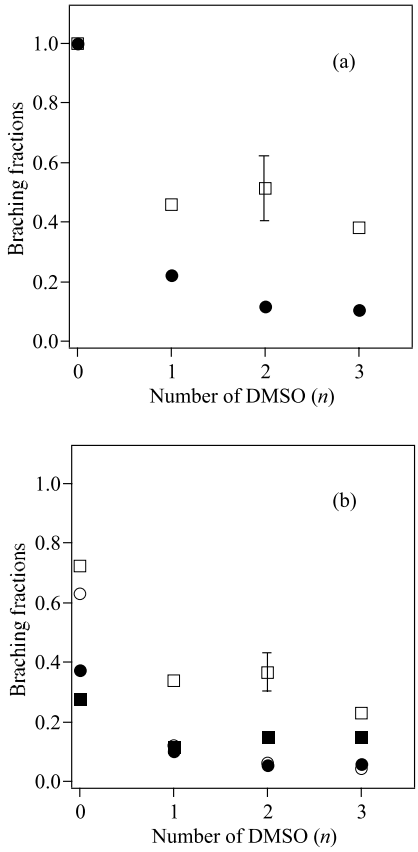


**Fig. 7.** (a) Branching fractions, $R_t$, for the photolysis of hemin$^+$(DMSO)$_n$ clusters are displayed as a function of $n$. Filled circles and empty squares indicate $R_t$ for the photolysis at 18 800 and 28 200 cm$^{-1}$, respectively. (b) Branching fractions, $R_1$ [$= I[-\mathrm{CM}]/\Sigma I_p$] and $R_2$ [$= I[-2\mathrm{CM}]/\Sigma I_p$], for the photolysis of the hemin$^+$(DMSO)$_n$ clusters are displayed as a function of $n$. Filled and empty circles indicate $R_1$ and $R_2$ for the photolysis at 18 800 cm$^{-1}$, respectively. Filled and empty squares indicate $R_1$ and $R_2$ for the photolysis at 28 200 cm$^{-1}$, respectively.

$m \leq n$) are not observed. This result seems to indicate that both the evaporation and $\beta$-cleavage reaction may take place competitively from the higher vibrational levels of the electronic ground state as discussed later (see Eqs. (8, 9)).

Figure 6 shows the total branching fractions of $\beta$-cleavage reaction, $R_t$, for $n = 1$ in the 15 800–20 000 cm$^{-1}$ region. $R_t$ is defined as

$$R_t = (I[-2\mathrm{CM}] + I[-\mathrm{CM}])/\Sigma I_p, \qquad (11)$$

where $I$[–CM] and $I$[–2CM] are the intensities of [hemin$^+$–$CH_2COOH$] and [hemin$^+$–2($CH_2COOH$)], respectively, and $\Sigma I_p$ is the total intensity of the product ions. This figure also shows the branching fractions of –CM, $R_1$ [$= I$[–CM]$/\Sigma I_p$], and −2CM, $R_2$ [$= I$[–2CM]$/\Sigma I_p$]. The ratios of these branching fractions, $R_1/R_2$, show no appreciable change in this energy region. These results seem to imply that the activation barrier height for the reaction from −CM to −2CM is not so high. On the other hand, the $R_t$ values increase suddenly in this energy region and show the threshold behavior at ∼17 200 cm$^{-1}$. From this energy, the upper limit of the dissociation energy for the $\beta$-cleavage, $V_{\mathrm{CM}}$, is determined as follow. Here, $V_{\mathrm{CM}}$ is related to the photon energy by

$$h\nu + E_1 \geq V_1 + V_{\mathrm{CM}} \qquad (12)$$

where $V_1$ is the binding energy and $E_1$ is the average internal energy of hemin$^+$(DMSO)$_1$ calculated by using the evaporative ensemble model. From the onset energy, $V_{\mathrm{CM}}$ is estimated as $\leq 2.5 \pm 0.3$ eV, which is much higher than the calculated activation energy of this reaction as discussed later.

In Figure 7a, the total branching fractions of $\beta$-cleavage reaction, $R_t$, are plotted as a function of $n$. As shown in the figure, $R_t$ decreases suddenly from $n = 0$ to 1 and it decreases further with much slower rate for $n = 1$–3. Although it is not shown, the total absorption cross-sections ($\sigma_{\mathrm{rel}}$) of these clusters at 18 800 cm$^{-1}$ are found to be almost the same. Thus these results indicate that the decomposition of hemin$^+$ at 18 800 cm$^{-1}$ is efficiently suppressed by the addition of a few solvent molecules. As seen in Figure 7a, the reactive fractions in the photodissociation at 28 200 cm$^{-1}$ are also affected by the solvation. However, the effect of solvation is rather

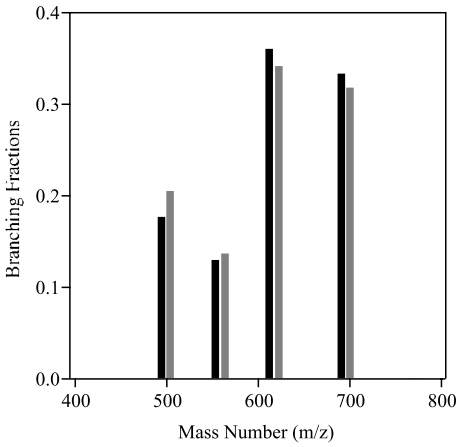


**Fig. 8.** Calculated branching fractions of the product ions for the photolysis of hemin$^+$(DMSO)$_3$ at 28 200 cm$^{-1}$ are presented as the filled bars. The observed branching fractions are also presented as striped bars for comparison.

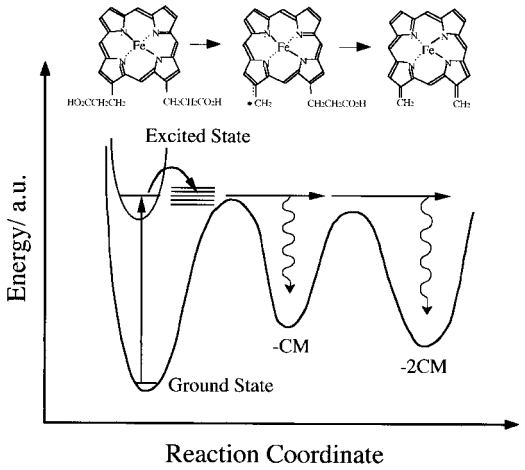


**Fig. 9.** Schematic potential energy curves of hemin$^+$ along the reaction coordinate of the ·$CH_2COOH$ release.

small comparing with that for the 18 800 cm$^{-1}$ excitation. Figure 7b shows the branching ratios for the first and second $\beta$-cleavage reaction, $R_1$ and $R_2$, for the photolysis of hemin$^+$(DMSO)$_n$ clusters recorded with irradiation of the 2nd and 3rd harmonic of YAG laser. As seen in this figure, $R_2$ at 28 200 cm$^{-1}$ is two times larger than that at 18 800 cm$^{-1}$. It is also worth noticing that the ratio of the $R_1$ and $R_2$ values at 18 800 cm$^{-1}$ does not change appreciably, though these values decrease gradually with increasing $n$. These results suggest that the first $\beta$-cleavage (Eq. (9)) is the rate-determining step.

In order to get further insight into the mechanism of $\beta$-cleavage reaction, the mass distribution of the photodissociation products for hemin$^+$(DMSO)$_3$ is simulated by RRK calculations with using the aforementioned binding energies and internal energies of the clusters. Figure 8 shows the calculated branching fractions for $n = 3$ at 28 200 cm$^{-1}$. The observed branching fractions are also shown for comparison. Although the calculations slightly underestimate the reactive fractions, the theoretical results agree well with the experimental fractions. From these analyses, the activation energies of the first (Eq. (9)) and the second $\beta$-cleavage (Eq. (10)) are estimated as 1.4 and 0.9 eV, respectively. These results are consistent with the observed features that the first $\beta$-cleavage is the rate-determining step and its branching ratio, $R_1$, is smaller than $R_2$, especially for the photolysis at 28 200 cm$^{-1}$. The calculated activation energies are substantially smaller than the upper limit of the dissociation energy for the $\beta$-cleavage of $n = 1$ ($V_{CM} \leq 2.5 \pm 0.3$ eV) estimated from the threshold energy of the reaction in Figure 6. Although it is difficult to compare these numbers without the knowledge on the solvation energy of the activation barrier height, a part of the difference in energies is due the large number of internal modes in hemin$^+$(DMSO)$_n$, which may require much higher excess energy than the activation energy of the reaction. Figure 9 shows the schematic potential energy curve along the $\beta$-cleavage reaction with including the above activation energies. The dissociation of a carboxymethyl group produces an intermediate with an unpaired electron as shown in equations (5, 9). This intermediate is stabilized as a result of the delocalization of unpaired electron in the $\pi$-electron network. A major driving force and stabilizing effect of the fragmentation of porphyrinic compounds is the formation of even-electron ion; the difference in stabilization between even- and odd-electron ions is accentuated by the macro-ring [41,44,45]. Because hemin$^+$ is the even-electron ion, release of two substituents to form even-electron fragment is much favorable for stabilizing the product ion. These arguments are consistent with the results of the RRK calculations mentioned previously; the dissociation energy of the second $\beta$-cleavage is estimated to be much smaller than that of the first one. Thus, the rate-determining step in the reaction to produce [hemin$-2CH_2COOH$]$^+$ from [hemin]$^+$ would be the first $\beta$-cleavage. This conclusion is also supported by the observations that the ratios, $R_1/R_2$, is not sensitive to the number of solvent molecules and the photon energy in this region.

As it is seen in Figure 5, the photolysis of hemin$^+$(DMSO)$_3$ at 18 800 cm$^{-1}$ also induces the reaction as in the case of $n = 2$. Since the binding energies between the hemin$^+$ ion and DMSO are as high as the activation energies, we would expect no reaction product for these clusters if the reaction takes place after the sequential evaporation is completed. The observation of the reaction products indicates that both the $\beta$-cleavage reaction and evaporation proceed competitively as shown in equations (8, 9). These arguments are also confirmed by the calculations on the product distribution as shown in Figure 8. As mentioned previously, we observe no solvated product ions such as [hemin$^+$–$k$($CH_2COOH$)](DMSO)$_m$ ($k = 1$ or 2, $m \leq n$) in the photolysis of hemin$^+$(DMSO)$_n$ as shown in Figure 5. This result seems to be in contradiction with the competitive nature of the reaction. One of the possible reasons for the absence of the solvated product ions may be a substantially large exothermicity of the $\beta$-cleavage reaction.

## 4 Conclusions

The metastable decomposition and the photodissociation of hemin$^+$(DMSO)$_n$ clusters produced with ESI have been studied by using a tandem mass-spectrometer. Using an evaporative ensemble model, the incremental binding energies of DMSO and average internal energies of clusters have been estimated. In the photodissociation of these clusters, the evaporation of solvents and the $\beta$-cleavage reactions to loss one and two carboxymethyl-groups have been found to be the dominant processes. From the analysis of the mass distributions of the product ions, both processes have been found to be the competitive processes. We have also carried out the RRK calculations on the product distribution. Both the experimental and theoretical results indicate that the first $\beta$-cleavage is the rate-determining process for the reaction of hemin$^+$(DMSO)$_n$ clusters.

The authors thank Professor J. Setsune for helpful discussions. This work is partially supported by the Grant-in-Aid (Grants #11304042) from the Ministry of Education, Science, Sports, and Culture of Japan, and by the Grant-in-Aid for Scientific Research (Grants #11740326, and #13640512) and a research grant for the Future Program from Japan Society for Promotion of Science. KF is also grateful to the Hyogo Science and Technology Association for partial financial supports.

## References

1. A.W. Castleman Jr, R.G. Keesee, Chem. Rev. **86**, 589 (1986)
2. M.T. Bowers, A.G. Marshall, F.W. McLafferty, J. Phys. Chem. **100**, 12897 (1996)
3. *Clusters of Atoms and Molecules*, edited by H. Haberland (Springer-Verlag, Heidelberg, 1994), Vol. I and II, and references cited therein
4. A.W. Castleman Jr, K.H. Bowen, J. Phys. Chem. **100**, 12911 (1996)
5. *Advances in Metal and Semiconductor Clusters*, edited by M.A. Duncan (JAI Press Inc., New York, 2001), Vol. 5, and references cited therein
6. O.M. Cabarcos, C.J. Weinheimer, J.M. Lisy, J. Phys. Chem. **103**, 8777 (1999)
7. J.A. Draves, Z. Luthey-Schulten, W.-L. Liu, J. M. Lisy, J. Chem. Phys. **93**, 4589 (1990)
8. K. Fuke, K. Hashimoto, S. Iwata, Adv. Chem. Phys. **110**, 431 (1999), and references cited therein
9. Y. Ohshima, O. Kajimoto, K. Fuke, in *Electron Transfer in Chemistry*, edited by Y. Haas (Wiley-VCH, 2001)
10. R. Takasu, F. Misaizu, K. Hashimoto, K. Fuke, J. Phys. Chem. A **101**, 3078 (1997)
11. R. Takasu, H. Ito, K. Nishikawa, K. Hashimoto, R. Okuda, K. Fuke, J. El. Sepctros. Relat. Phenom. **106**, 127 (2000)
12. C. Nitsch, Chr. Hüglin, I.V. Hertel, C.P. Schulz, J. Chem. Phys. **101**, 6559 (1994)
13. C.P. Schulz, C. Nitsch, J. Chem. Phys. **107**, 9794 (1997)
14. P. Brockhaus, I.V. Hertel, C.P. Schulz, J. Chem. Phys. **110**, 393 (1999)
15. M. Sanekata, F. Misaizu, K. Fuke, J. Chem. Phys. **104**, 9768 (1996)
16. F. Misaizu, M. Sanekata, K. Fuke, J. Chem. Phys. **100**, 1161 (1994)
17. M.A. Duncan, Ann. Rev. Phys. Chem. **48**, 69 (1997)
18. M.H. Shen, J.M. Farrar, J. Chem. Phys. **94**, 3322 (1991)
19. J. Martin, E. Quirke, in *The Porphyrin handbook*, edited by K.M. Kadish, K.M. Smith, R. Guilard (Academic Press, San Diego, 2000), Vol. 7, Sect. 54
20. *Electrospray Ionization Mass Spectrometry*, edited by R.B. Cole (Wiley, New York, 1997)
21. C.M. Whitehouse, R.N. Dreyer, M. Yamashita, J.B. Fenn, Anal. Chem. **57**, 675 (1985)
22. T. Blades, P. Jayaweera, M.G. Ikonomou, P. Kebarle, J. Chem. Phys. **92**, 5900 (1990)
23. R.D. Smith, J.A. Loo, C.G. Edmonds, C.J. Barinaga, H.R. Udseth, Anal. Chem. **62**, 882 (1990)
24. T.G. Spence, T.D. Burns, G.B. Guckenberger, L.A. Posey, J. Phys. Chem. **101**, 1081 (1997)
25. C.J. Thompson, J. Husband, F. Aguirre, R.B. Metz, J. Phys. Chem. **104**, 8155 (2000)
26. X.-B. Wang, L.-S. Wang, J. Chem. Phys. **111**, 4497 (1999)
27. K. Kalyanasundaram, *Photochemistry of Polypyridine and Porphyrin Complexes* (Academic Press, London, 1992), and references cited therein
28. *The Porphyrin handbook*, edited by K.M. Kadish, K.M. Smith, R. Guilard (Academic Press, San Diego, 2000), and references cited therein
29. *The Porphyrins*, edited by D. Dolphin (Academic Press, New York, 1978), and references cited therein
30. G.J. van Berkel, S. A. McLuckey, G. Glish, Anal. Chem. **63**, 1098 (1991)
31. S. Nonose, H. Tanaka, K. Fuke, Int. J. Mass Spetrom., submitted
32. C.E. Klots, J. Phys. Chem. **92**, 5854 (1988)
33. J.A. Shelnutt, in *The Porphyrin handbook*, edited by K.M. Kadish, K.M. Smith, R. Guilard (Academic Press, San Diego, 2000), Vol. 7, Sect. 50
34. T.B. Douglas, J. Am. Chem. Soc. **70**, 2001 (1948)
35. J. Sunner, P. Kebarle, J. Am. Chem. Soc. **106**, 6135 (1984)
36. M. Gouterman, J. Mol. Spectrosc. **6**, 138 (1961)
37. L. Edwards, D. Dolphin, M. Gouterman, A.D. Adler, J. Mol. Spectrosc. **38**, 16 (1971)
38. M. Gouterman, in *The Porphyrins*, edited by D. Dolphin (Academic Press, New York, 1978), Vol. 3
39. Y.-K. Choe, T. Hashimoto, H. Nakano, K. Hirao, Chem. Phys. Lett. **295**, 380 (1998)
40. A. Ghosh, in *The Porphyrin handbook*, edited by K.M. Kadish, K.M. Smith, R. Guilard (Academic Press, San Diego, 2000), Vol. 7, Sect. 47
41. F.W. McLafferty, *Interpretation of Mass Spectra*, 3rd edn. (University Science Books, Mill Valley, California, 1980)
42. K.D. Stanley, R. Lopez de la Vega, J.M.E. Quirke, B.D. Beato, R.A. Yost, Chem. Geol. **91**, 169 (1991)
43. B.D. Beato, R.A. Yost, J.M.E. Quirke, Chem. Geol. **91**, 185 (1991)
44. K.M. Smith, in *Porphyrins and Metalloporphyrins*, edited by K.M. Smith (Elsevier, Amsterdam, 1975), pp. 381-398
45. H. Budzikiewicz, in *The Porphyrins*, edited by D. Dolphin (Academic Press, New York, 1978), pp. 395-459
46. R.C. Dougherty, in *Biochemical Applications of Mass Spectrometry*, edited by G.R. Waller (Wiley, New York, 1972)